

Using ZnCo_2O_4 Nanoparticles as The Hole Transport Layer to Improve Long-Term Stability of Perovskite Solar Cells

Bo-Rong Jheng

National Yang Ming Chiao Tung University

Pei-Ting Chiu

Industrial Technology Research Institute

Sheng-Hsiung Yang (✉ yangsh@mail.nctu.edu.tw)

National Yang Ming Chiao Tung University

Yung-Liang Tong

Industrial Technology Research Institute

Research Article

Keywords: ternary metal oxide, ZnCo_2O_4 , hole transport layer, perovskite solar cells, long-term stability.

Posted Date: January 10th, 2022

DOI: <https://doi.org/10.21203/rs.3.rs-1145111/v2>

License:  This work is licensed under a Creative Commons Attribution 4.0 International License.

[Read Full License](#)

Version of Record: A version of this preprint was published at Scientific Reports on February 21st, 2022.

See the published version at <https://doi.org/10.1038/s41598-022-06764-w>.

Abstract

Inorganic metal oxides with the merits of high carrier transport capability, low cost and superior chemical stability have largely served as the hole transport layer (HTL) in perovskite solar cells (PSCs) in recent years. Among them, ternary metal oxides gradually attract attention because of the wide tenability of the two inequivalent cations in the lattice sites that offer interesting physicochemical properties. In this work, ZnCo_2O_4 nanoparticles (NPs) were prepared *by a chemical precipitation method and served* as the HTL in inverted PSCs. The device based on the ZnCo_2O_4 NPs HTL showed better efficiency of 12.31% and negligible hysteresis compared with the one using PEDOT:PSS film as the HTL. Moreover, the device sustained 85% of its initial efficiency after 240 hours storage under a halogen lamps matrix exposure with an illumination intensity of 1000 W/m^2 , providing a powerful strategy to design long-term stable PSCs for future production.

1. Background

Perovskite solar cells (PSCs) have attracted a great deal of attention from academic and industrial researchers because of their rapid development in power conversion efficiency (*PCE*) from 3.8–25.5% within a decade [1, 2]. Perovskites are considered as ideal photovoltaic materials in solar cells due to their high absorption in the visible spectrum [3], long carrier diffusion length [4], high carrier mobility [5], low exciton binding energy [6], tunable bandgaps by exchanging atomic composition [7, 8], large area production and low cost owing to solution processability. In recent years, PSCs using multiple-cation lead halide as the absorbing layer dominate mainly because of their high stability and high reproducibility compared to single-cation perovskites like MAPbI_3 , FAPbI_3 , and CsPbI_3 . Saliba et al. reported a triple-cation perovskite material $\text{Cs}_x(\text{FA}_{0.17}\text{MA}_{0.83})_{1-x}\text{Pb}(\text{I}_{0.83}\text{Br}_{0.17})_3$ as the active layer for fabricating PSCs [9]; the best device showed an optimized open-circuit voltage (V_{OC}) of 1147 mV, a short-circuit current density (J_{SC}) of 23.5 mA/cm^2 , a fill factor (*FF*) of 0.785, and a certified *PCE* of 21.17%. Moreover, the device showed a stabilized *PCE* which slowly dropped to 18% after 250 hours under full illumination at room temperature. Bu et al. utilized a quadruple-cation perovskite material $\text{K}_y(\text{Cs}_{0.05}(\text{FA}_{0.85}\text{MA}_{0.15})_{0.95})_{1-y}\text{Pb}(\text{Br}_{0.15}\text{I}_{0.85})_3$ as the absorbing layer [10]. The optimized device achieved a high *PCE* of 20.56%, a V_{OC} of 1,132 V, a J_{SC} of 22.95 mA/cm^2 , and a *FF* of 0.79. Besides, the device exhibited stable conversion efficiency over 1000 hours stored under ambient air ($10 \pm 5 \text{ RH}\%$) without encapsulation. Hence, the utilization of multiple-cation perovskite material was adopted as the light absorber instead of single- or double-cation perovskites.

In recent years, inverted PSC (n-i-p) has been extensively investigated because of its simple device architecture, ease of fabrication, improved stability, and reduced hysteresis effect [11]. Besides, tandem cells with augmented efficiency can be accomplished by combing inverted PSCs with traditional solar cells such as silicon or copper indium gallium selenide solar cells [12, 13]. To fabricate inverted PSCs, organic polymers such as poly(3,4-ethylenedioxythiophene):poly(styrene sulfonate) (PEDOT:PPS), poly(4,4'-bis(*N*-carbazolyl)-1,10-biphenyl) (PPN), poly (*p*-phenylene) (PPP), and polythiophene (PT) have

been used as the hole transport layer (HTL) [14–16]. The acidic and hygroscopic nature of PEDOT:PSS induces corrosion of transparent conducting oxides such as fluorine-doped tin oxide (FTO), which restricts the long-term stability and commercialization of inverted PSCs [17, 18]. These polymers cause challenges due to a susceptibility to environmental factors such as moisture and ultraviolet light exposure. Furthermore, the complicated synthesis and purification process of these materials make them very expensive and difficult for mass production. In contrast to organic polymers, inorganic hole transport materials have the advantages of high carrier mobility, superior stability, low cost, and facile preparation, such as vanadium oxide [19], copper oxide [20], nickel oxide [21], and cobalt oxide (Co_3O_4) [22]. Bashir et al. utilized spinel Co_3O_4 NPs as the HTL for the fabrication of PSCs with a large-area of 70 cm^2 to achieve a *PCE* of 11.06% and extensive stability up to 2500 hours under standard one sun illumination. In addition to those common metal oxides, spinel ternary metal oxides prepared by solution process have been gradually investigated as promising hole conductors in optoelectronics and lithium- CO_2 batteries due to their tunable optical and electrical properties [23–25]. Choy and co-workers firstly proposed a controllable deamination strategy to synthesize nickel cobaltite (NiCo_2O_4) NPs as the HTL in inverted PSCs [26]. The optimal NiCo_2O_4 -based cell showed 18.23% efficiency with negligible hysteresis. Lee et al. demonstrated solution-processed copper cobaltite (CuCo_2O_4) as the HTL to fabricate high-efficiency inverted PSCs [27]. The best PSC revealed a *PCE* of 14.12% with negligible hysteresis and retained 71% of initial *PCE* after 96 hours storage under a continuous yellow light irradiation. Apart from spinel NiCo_2O_4 and CuCo_2O_4 , ZnCo_2O_4 has also been reported to possess several features of hole transport ability, wide optical bandgap, and solution processability [28, 29], which can serve as the photocathode for the applications in photoelectrochemical water splitting and lithium-ion batteries [30, 31]. Despite being a good candidate for alternative HTLs, surprisingly, no study about the use of ZnCo_2O_4 as the HTL in PSCs has been reported so far. Therefore, for the first time, we attempted to prepare ZnCo_2O_4 NPs as an efficient HTL in PSCs, which may bring important contribution to long-term stability and enhanced photovoltaic performance of PSCs due to its inorganic and hole transport nature.

In this research, ammonia was chosen as a soft base to prepare ZnCo_2O_4 NPs as the HTL instead of strong bases like sodium hydroxide. The as-prepared ZnCo_2O_4 NPs can be cast into uniform thin films with high optical transparency and decent electrical properties, which are comparable or even better than PEDOT:PSS film. To fabricate inverted PSCs, [6, 6]-phenyl- C_{61} -butyric acid methyl ester (PC_{61}BM) doped with tetrabutylammonium tetrafluoroborate (TBABF_4) and polyethylenimine (PEI) were chosen as the electron transport layer (ETL). The device with the configuration of FTO/HTL/perovskite/ TBABF_4 -doped PC_{61}BM /PEI/Ag was fabricated and evaluated, while ZnCo_2O_4 NPs layer or PEDOT:PSS film were used as the HTL for comparison. Our results demonstrated the best *PCE* value up to 12.31% and nearly hysteresis-free photocurrents at different scan directions and voltage sweep rates when using ZnCo_2O_4 NPs layer as the HTL. Moreover, the device sustained 85% of its initial efficiency after 240 hours storage under a halogen lamps matrix exposure with an illumination intensity of 1000 W/m^2 , revealing superior potential in photovoltaic application.

2. Experimental Section

2.1 Materials. FTO-coated glass substrates ($7 \Omega/\text{square}$) were purchased from Ruilong Optoelectronics Technology Co., Ltd. from Taiwan. Cobalt(II) nitrate hexahydrate ($\text{Co}(\text{NO}_3)_2 \cdot 6\text{H}_2\text{O}$, purity 98-102%) and zinc(II) nitrate hexahydrate ($\text{Zn}(\text{NO}_3)_2 \cdot 6\text{H}_2\text{O}$, purity 99%) were purchased from Alfa Aesar. Aqueous ammonium hydroxide ($\text{NH}_4\text{OH}_{(\text{aq})}$, 25–28 wt%) was bought from Sigma-Aldrich. High-purity perovskite precursors including lead iodide (PbI_2 , purity 99.999%), lead bromide (PbBr_2 , purity 99.99%), and cesium iodide (CsI , purity 99.9%) were purchased from Alfa Aesar. Methylammonium bromide (MABr , purity 98.0%) was bought from TCI. Formamidinium iodide (FAI , purity 98%) was brought from STAREK Scientific Co., Ltd. from Taiwan. PEDOT:PSS aqueous solution (Clevios P VP Al 4083) was purchased from Heraeus Precious Metals GmbH & Co. KG. PEI (molecular weight 25,000) was bought from Sigma-Aldrich. PC_{61}BM (purity 99%) was purchased from Solenne B.V., Netherlands. Other chemicals and solvents were bought from Alfa Aesar, Acros or Sigma-Aldrich and used without further purification.

2.2 Synthesis of ZnCo_2O_4 NPs. The ZnCo_2O_4 NPs were prepared by a chemical precipitation method. $\text{Co}(\text{NO}_3)_2 \cdot 6\text{H}_2\text{O}$ (0.9312 g, 3.2 mmol) was dissolved in 16 mL of deionized (DI) water with stirring at room temperature, and $\text{NH}_4\text{OH}_{(\text{aq})}$ (4.8 mL) was added dropwise into the above solution. After being sonicated for 10 min, 8 mL of $\text{Zn}(\text{NO}_3)_2 \cdot 6\text{H}_2\text{O}$ aqueous solution (0.2 M in DI water) was subsequently added and stirred for 30 min. The mixture was heated to 150°C to evaporate all solvent in the air and then sintered at 225°C for 2 hr. The synthesized ZnCo_2O_4 NPs were washed twice with DI water and dried at 60°C for 4 hr. To prepare $\text{ZnCo}_2\text{O}_4/\text{DI}$ water dispersion, 50 mg of ZnCo_2O_4 NPs were dispersed in 2 mL of DI water under ultrasonicated treatment for 2 hr. It is important to note that all above solutions were freshly prepared before the device fabrication.

2.3 Device fabrication. The final device structure is FTO/ ZnCo_2O_4 NPs or PEDOT:PSS/perovskite/TBABF₄-doped PC_{61}BM /PEI/Ag. FTO were partially removed from the substrate via etching with zinc powder and $2\text{M HCl}_{(\text{aq})}$ to generate the desired pattern. The patterned FTO substrates were cleaned stepwise in detergent, DI water, acetone, and isopropyl alcohol (IPA) under ultrasonication for 10 min each. Afterward, the FTO substrates were dried with a nitrogen flow and followed by ultraviolet (UV)-ozone exposure for 20 min. The prepared ZnCo_2O_4 dispersion in DI water was spin-coated on cleaned FTO glass substrates at 2000 rpm for 30 sec, followed by drying at 200°C for 15 min. For comparison, PEDOT:PSS film on the FTO substrate was prepared via spin coating at 7000 rpm for 40 sec and then dried at 150°C for 15 min. After transferring substrates into the nitrogen-filled glovebox, the perovskite solution was spin coated onto the ZnCo_2O_4 or PEDOT:PSS layers. For the perovskite $\text{Cs}_{0.05}\text{FA}_{0.8}\text{MA}_{0.15}\text{Pb}(\text{Br}_{0.15}\text{I}_{0.85})_3$ solution used in this research, a mixture of CsI (17.5 mg), FAI (197 mg), MABr (23.8 mg), PbI_2 (555.2 mg), and PbBr_2 (78 mg) was dissolved in a mixed solvent (1 mL) consisting of *N,N*-dimethylformamide and dimethyl sulfoxide with a 4:1 volume ratio at 70°C for 1 hr with stirring, followed by filtration with $0.45 \mu\text{m}$ membrane filters before device fabrication. The perovskite solution was spin coated on the substrates with a spinning speed of 1200 rpm for 10 sec and 4500 rpm

for 20 sec. After 5 sec in the second spinning step, 300 μL of the anti-solvent ethyl acetate was dropped. The resulting perovskite films were annealed at 105°C for 1 hr. The PC₆₁BM solution (20 mg/mL in chlorobenzene containing 0.04 mg of tetrabutylammonium tetrafluoroborate, TBABF₄) was spin coated at 3000 rpm for 30 sec on top of the perovskite layer and then dried at 100°C for 10 min. The PEI solution (0.1 wt% in IPA) was spin coated on top of the PC₆₁BM layer at 5000 rpm for 30 sec. Finally, Ag electrodes with a thickness of 100 nm were thermally evaporated on top of the PEI layer under a base pressure of 10⁻⁶ Torr. The active area of each device was defined by a shadow mask with an open area of 4.5 mm².

2.4 Characterization and Measurement. The top-view and cross-section micrographs of samples were investigated with an ultrahigh-resolution ZEISS AURIGA Crossbeam scanning electron microscope (SEM). The surface morphology and roughness of ZnCo₂O₄ films were measured by a Bruker Innova atomic force microscope (AFM). The morphology and size of ZnCo₂O₄ NPs were examined with a JEOL JEM-1400 transmission electron microscope (TEM). The Fourier transform infrared (FT-IR) spectra of ZnCo₂O₄ pellets were measured using a Thermo Scientific Nicolet iS-10 spectrometer. The ultraviolet photoelectron spectroscopy (UPS) measurement for ZnCo₂O₄ NPs was performed on a PHI 5000 VersaProbe \square spectrometer. A He I ($h\nu = 21.22$ eV) discharge lamp was used as the excitation source. X-ray photoelectron spectroscopy (XPS) measurements were conducted by the same spectrometer for elemental composition analysis of ZnCo₂O₄ NPs. X-ray diffraction (XRD) patterns and crystallinity of samples were obtained from a Rigaku MiniFlex \square X-ray diffractometer. The steady-state photoluminescence (PL) spectra of perovskites on the FTO, PEDOT:PSS, or ZnCo₂O₄ were measured using a Princeton Instruments Acton 2150 spectrophotometer. A KIMMON KOHA He–Cd laser with double excitation wavelengths at 325/442 nm was utilized as the light source. The absorption and transmission spectra of samples were recorded with the same spectrophotometer using a xenon lamp (ABET Technologies LS 150) as the light source. To perform time-resolved PL (TR-PL) measurements, a 473 nm pulsed laser (Omicron) was utilized as an excitation light source. The TR-PL signals were recorded by a time-correlated single-photon counting module (PicoQuant MultiHarp 150 4N) combined with a photomultiplier tube through an Andor Kymera 328i spectrometer. The apparatus was assembled by LiveStrong Optoelectronics Co., Ltd. from Taiwan. The current density-voltage (J-V) characteristics of the PSCs were measured under ambient environment by using a Keithley 2401 source measuring unit under AM 1.5G simulated sunlight exposure (Yamashita Denso YSS-100A equipped with a xenon short arc lamp, 1000 W) at 100 mW/cm². The scan rate for J-V measurements was 20 mV/s. The external quantum efficiency (EQE) measurements were conducted using a PV Measurement QE-R instrument which was assembled by Enli Technology Co., Ltd. from Taiwan. To exploit the stability of devices, the encapsulated PSCs were constantly exposed to a halogen lamps matrix with an illumination intensity of 1000 W/m² at room temperature with 40–60% relative humidity and their J-V characteristics were measured in each 24-hr period.

3. Results And Discussion

3.1. Characterization of ZnCo_2O_4 NPs. Crystallographic information of the prepared ZnCo_2O_4 NPs was acquired and the corresponding pattern is shown in Figure 1(a). The diffraction signals of ZnCo_2O_4 are found at $2\theta = 31.06^\circ, 36.7^\circ, 38.36^\circ, 44.72^\circ, 55.52^\circ, 59.1^\circ,$ and 64.96° , corresponding to the (220), (311), (222), (400), (422), (511), and (440) planes, respectively [32, 33]. According to the XRD pattern, the prepared ZnCo_2O_4 is well consistent with the spinel phase. Figure 1(b) displays the TEM image of ZnCo_2O_4 NPs. These particles tend to aggregate with an average diameter of 20 nm.

The residual NH_3 molecules on the surface of ZnCo_2O_4 may deteriorate its electrical properties and thus should be removed. The FT-IR experiment was adopted to detect the removal of NH_3 , and the corresponding infrared spectra before and after calcination are depicted in Figure 2. Before calcination, the characteristic stretching bands of NH_3 molecules were observed at $3655\text{--}2597, 1753,$ and 826 cm^{-1} , which are assigned to the N–H stretching mode, H–N–H bending vibration, and H–N–H rocking mode, respectively [34]. A significant absorption band was found at 1317 cm^{-1} , which was attributed to NO_3 groups from starting materials [35]. In addition, the two IR absorption peaks for the Zn–O and Co–O bonds were revealed at 685 and 561 cm^{-1} , respectively [36]. After calcination, it is clearly seen that the absorption bands at $3655\text{--}2597, 1753,$ and 826 cm^{-1} were vanished, indicating that NH_3 molecules were removed. The NO_3 absorption signal was also greatly diminished and a trace was found at 1384 cm^{-1} . The Zn–O and Co–O bonds still existed at similar positions. The results proved that NH_3 molecules can be easily removed during annealing to further improve electrical properties of ZnCo_2O_4 NPs.

To identify the Zn:Co ratio in our prepared ZnCo_2O_4 NPs, the XPS measurements were carried out. Figure 3(a) shows the Co $2p$ band of ZnCo_2O_4 , and the multicomponent band can be deconvoluted into four different states at $779.5 (2p_{3/2}), 794.7 (2p_{1/2})$ for Co^{3+} , and $780.6 (2p_{3/2}), 795.7\text{ eV} (2p_{1/2})$ for Co^{2+} , and two shake-up satellite peaks at 789.8 eV near Co $2p_{3/2}$ band and 804.9 eV near Co $2p_{1/2}$ band. The locations of these states are in good accordance with the previous literature [37, 38]. The Zn $2p$ band of the spinel ZnCo_2O_4 NPs is depicted in Figure 3(b), revealing two XPS peaks at $1021 (2p_{3/2})$ and $1044\text{ eV} (2p_{1/2})$ for Zn^{2+} [38]. The Zn:Co atomic ratio is calculated to be 1:2.19 based on the XPS band area, which is close to the designed ratio of ZnCo_2O_4 (Zn:Co = 1:2). H.Y. Chen and his coworker claimed that some Co^{3+} can occupy Co^{2+} or Zn^{2+} sites in the structure because of the similar ionic radii of Co and Zn, thus giving rise to the antisite defects (Zn_{Co}) [39], which is energetically favored for p -type conductivity. The prepared ZnCo_2O_4 NPs in this study is expected to show similar feature that is beneficial for carrier transport in optoelectronic devices. The O $1s$ spectrum of the obtained spinel ZnCo_2O_4 NPs is shown in Figure 3(c). The main signal due to lattice oxygen (O^{2-}) is observed at 529.4 eV that is in agreement with the previous report [40]. Besides, shoulder signals at a higher binding energy of 530.9 eV and 532.3 eV come from surface hydroxyl groups and chemisorbed oxygen [41].

The energy levels of ZnCo_2O_4 NPs were calculated from their UPS spectra, as shown in Figure 4. The work function (ϕ_w) is derived by subtracting the binding energy cutoff in the high binding energy region

(around 16.71 eV) from He I photon energy (21.22 eV). Since the ϕ_w is defined as the energy difference between the Fermi level (E_F) and the vacuum level (0 eV), the E_F value of ZnCo_2O_4 NPs is determined to be -4.51 eV from Figure 4(a). Furthermore, the binding energy cutoff in the low binding energy region reveals the energy difference between the E_F and the valence band (VB) level [42]. The low energy binding cutoff of ZnCo_2O_4 NPs is found at around 0.6 eV in Figure 4(b), indicative of its VB level at -5.08 eV. Compared with the PEDOT:PSS film (VB level = -5.02 eV) [43], the downshifted VB level of ZnCo_2O_4 NPs is matched better with the perovskite absorbing layer, which can improve the hole extraction from the perovskite to ZnCo_2O_4 HTL.

3.2. Morphological observation of the ZnCo_2O_4 and perovskite layers. The top-view SEM images of PEDOT:PSS or ZnCo_2O_4 NPs deposited on the FTO substrates are shown in Figures 5(a) and (b), respectively. PEDOT:PSS is a transparent polymer and hence the grains of low-lying FTO are clearly seen. Besides, many small cracks exist on the surface of PEDOT:PSS. In Figure 5(b), ZnCo_2O_4 NPs are homogeneously deposited on the FTO surface and the grains of FTO are not observable. The surface roughness of the ZnCo_2O_4 /FTO substrate may become lower since the grains of FTO are completely covered by ZnCo_2O_4 NPs, as compared with the PEDOT:PSS/FTO substrate. To verify this, AFM technique was adopted to investigate the morphology and average roughness (R_a) of the prepared samples. Figures 5(c) and (d) show the topographic AFM images of PEDOT:PSS and ZnCo_2O_4 NPs on the FTO substrates, respectively, revealing similar morphological features to those of the top-view SEM images. Furthermore, the R_a values of PEDOT:PSS or ZnCo_2O_4 NPs deposited on the FTO are estimated to be 15.1 and 6.65 nm, respectively. The result reveals that ZnCo_2O_4 NPs can serve as a better surface modifier for FTO substrates than PEDOT:PSS, which is beneficial for improving interfacial contact and hole extraction between ZnCo_2O_4 NPs and the perovskite [44]. The cross-sectional SEM images of ZnCo_2O_4 NPs layer and PEDOT:PSS film can be seen in Figure S1(a) and (b) in the Supplementary Information, the thickness of ZnCo_2O_4 NPs layer and PEDOT:PSS film were estimated to be *ca.* 65 nm and *ca.* 40 nm, respectively.

Figures 6(a) and (b) show the top-view SEM images of the perovskite deposited on PEDOT:PSS or ZnCo_2O_4 NPs, respectively. No pinholes could be found for both perovskite films. The grain size of perovskite crystals on PEDOT:PSS is estimated to be in the range of 100–180 nm, while larger perovskite crystals with grain sizes of 200–300 nm were observed on ZnCo_2O_4 NPs, as shown in Figure 6(b). As mentioned in the previous part, the lower surface roughness of the ZnCo_2O_4 layer helps to form larger sizes of perovskite grains, as compared with PEDOT:PSS film [45]. The high-quality perovskite film grown on ZnCo_2O_4 NPs is expected to exhibit higher photocurrent and conversion efficiency of PSCs.

3.3. Electrical Investigation of ZnCo_2O_4 NPs and PEDOT:PSS film. To investigate the hole transport ability of ZnCo_2O_4 NPs and PEDOT:PSS film, hole-only devices with the structure of FTO/ ZnCo_2O_4 NPs or PEDOT:PSS/Ag were fabricated and evaluated. The electron-only device with the configuration of FTO/TBABF₄-doped PC₆₁BM/PEI/Ag was also fabricated for comparison. The corresponding current-

voltage characteristics of the three devices are depicted in Figure 7, indicating that the ZnCo₂O₄ NPs device exhibits higher current and better hole transport capability than PEDOT:PSS film. Figure S2 in the Supplementary Information displays hole mobility (μ_h) of ZnCo₂O₄ NPs and PEDOT:PSS film, which is inferred from the space-charge limited current equation $J = (9/8)\epsilon\epsilon_0\mu_h(V^2/L^3)$. The μ_h values of ZnCo₂O₄ NPs layer and PEDOT:PSS film are calculated to be 9.14×10^{-2} and 8.52×10^{-5} cm²/Vs, respectively. The obtained μ_h of PEDOT:PSS film is close to the reported value in the literature [46]. It is seen that our ZnCo₂O₄ NPs layer has a hole mobility by 3 orders of magnitude higher than that of the PEDOT:PSS film. Moreover, we found that the device FTO/TBABF₄-doped PC₆₁BM/PEI/Ag shows similar current-voltage behavior to the one based on ZnCo₂O₄ NPs, implying equivalent carrier transport capabilities of holes and electrons in our final inverted device architecture of FTO/ZnCo₂O₄ NPs/perovskite/TBABF₄-doped PC₆₁BM/PEI/Ag. The balanced carrier transport also helps to reduce the hysteresis effect of devices.

3.4. Optical Investigation of ZnCo₂O₄ NPs and Perovskite Layers. Figure S3(a) in the Supplementary Information shows the transmission spectra of the ZnCo₂O₄ NPs layer and PEDOT:PSS film from 315 to 750 nm. The transmittance was measured to be 55–90% in the range of 375–650 nm and even higher over 90% in the range of 650–750 nm for both samples with similar spectral shapes. Therefore, we speculate that the amount of incident photons entering into devices is close. The absorption spectrum of the ZnCo₂O₄ NPs layer is shown in Figure S3(b) and its optical bandgap (E_g) of 3.7 eV was estimated from the absorption edge around 335 nm. From UPS and absorption measurements, the conduction band (CB) level of ZnCo₂O₄ NPs is determined to be -1.38 eV, while the lowest-unoccupied molecular orbital (LUMO) of PEDOT:PSS is referred to the previous literature (LUMO = -3.4 eV) [47]. The relatively high CB level of ZnCo₂O₄ NPs can reduce electron transport from the perovskite to FTO and carrier recombination inside devices.

The steady-state PL spectra of the perovskite on the FTO substrate, PEDOT:PSS film, and ZnCo₂O₄ NPs layer are indicated in Figure 8(a). It is clearly seen that the perovskite deposited on the FTO substrate has the highest PL intensity, while the one on the ZnCo₂O₄ NPs layer owns the lowest PL emission. The reduced PL emission implies hindrance of electron-hole pair recombination and improvement of J_{SC} and FF of PSCs [27, 48]. Furthermore, the TR-PL decay experiment was performed and the obtained PL decay curves of the perovskite on FTO, PEDOT:PSS film, and ZnCo₂O₄ NPs layer are shown in Figure 8(b). The PL decay curves agree well with a biexponential decay fitting and corresponding lifetimes of τ_1 , τ_2 , and τ_{avg} are listed in Table S1 in the Supplementary Information. It is reported that fast decay (τ_1) originates from nonradiative capture of free carriers and the slow decay (τ_2) comes from radiative recombination of remaining excitons [27]. The τ_{avg} is determined by the equation $\tau_{avg} = \sum_i(A_i\tau_i^2)/\sum_i(A_i\tau_i)$, where A_i values is derived from the fitted curve data [49]. Generally, the shorter carrier lifetime indicates more efficient charge extraction. The τ_{avg} value of the perovskite on FTO was calculated to be 107.17 ns, and it decreased to 88.61 and 39.98 ns when the perovskite was deposited on the PEDOT:PSS film and

ZnCo₂O₄ NPs layer, respectively. This result indicates more effective charge extraction by the ZnCo₂O₄ NPs layer from the perovskite active layer as compared with the PEDOT:PSS film.

3.5. Device Evaluation. The p-i-n device structure of the inverted PSC based on ZnCo₂O₄ NPs HTL is shown in Figure 9(a), revealing a sandwiched architecture of FTO/ZnCo₂O₄ NPs/Cs_{0.05}FA_{0.8}MA_{0.15}Pb(Br_{0.15}I_{0.85})₃/TBABF₄-doped PC₆₁BM/PEI/Ag. Figure 9(b) shows the cross-sectional SEM micrograph of the whole device, revealing the thickness of FTO, ZnCo₂O₄ NPs layer, perovskite, PC₆₁BM+PEI, and Ag electrode to be 500, 60, 550, 35, and 135 nm, respectively. The energy level diagram of the whole device is illustrated in Figure 9(c). The VB and CB levels of ZnCo₂O₄ NPs have been discussed in the previous part, while the energy levels of the other components were referred to the previous reports [43, 50, 51]. In our device architecture, electrons can be successfully extracted from the perovskite absorber and transport to the Ag electrode through PC₆₁BM+PEI, while holes migrate gradually from the perovskite layer through ZnCo₂O₄ NPs and are collected on the FTO electrode. The J-V curves of the devices measured under AM 1.5 G are shown in Figure 9(d), and the measured parameters including J_{SC} , V_{OC} , FF , PCE , and series resistance (R_S) are summarized in Table 1. The optimized device based on ZnCo₂O₄ NPs showed a V_{OC} of 0.92 V, a J_{SC} of 19.85 mA/cm², a FF of 67.19%, and a PCE of 12.31% in the reverse scan, which is significantly higher than the one based on PEDOT:PSS (V_{OC} = 0.79 V, J_{SC} = 17.23 mA/cm², FF = 59.77%, and PCE = 8.11%). The statistical distribution of 20 individual devices for all photovoltaic parameters is depicted in Figure S4 in the Supplementary Information. It can be seen that our devices possessed good reproducibility and PSCs based on ZnCo₂O₄ NPs showed relatively higher photovoltaic parameters. The improved device performance is mainly ascribed to the increased J_{SC} value and energy level matching between ZnCo₂O₄ NPs/perovskite interface. Hysteresis index (HI) can be used to describe the hysteresis behavior of PSCs according to the equation $HI = (PCE_{reverse} - PCE_{forward}) / PCE_{reverse}$ [52]. The PSC based on ZnCo₂O₄ NPs has a smaller HI value of 0.043 as compared with that based on PEDOT:PSS (HI = 0.36). As a result, the reduced hysteresis of the PSC based on ZnCo₂O₄ NPs is in accordance with electrical measurements in the previous part. The normalized PCE evolution of the PSCs based on ZnCo₂O₄ NPs and PEDOT:PSS is shown in Figure 9(e) for comparison. The PSC based on ZnCo₂O₄ HTL retained 85% of its initial efficiency after 240 hours storage under a halogen lamps matrix exposure at room temperature, whereas the PCE of the device based on PEDOT:PSS HTL dropped to only 0.5% of its initial efficiency after 144 hours storage. Such fast deterioration can be attributed to the acidic nature of PEDOT:PSS causing corrosion to the perovskite and FTO substrate. Therefore, the use of inorganic ZnCo₂O₄ HTL is highly beneficial for the device stability. As mentioned in the Introduction, the device using CuCo₂O₄ as the HTL retained 71% of initial PCE after 96 hours storage under a continuous yellow light irradiation.²⁷ Our result reveals that ZnCo₂O₄ is a better candidate for the fabrication of stable PSCs. Figure 9(f) shows the EQE spectra and integrated current density of devices as a function of wavelength using ZnCo₂O₄ NPs and PEDOT:PSS as the HTL. The results demonstrate that the device based on ZnCo₂O₄ NPs has a higher photon-to-electron conversion capability from 300 to 750 nm compared to that based on PEDOT:PSS. The integrated current density for

the devices based on ZnCo₂O₄ NPs and PEDOT:PSS was calculated to be 18.4 and 15.45 mA/cm², respectively, which are similar to the J_{SC} values in Table 1.

Table 1
Device performance of all PSCs based on PEDOT:PSS film or ZnCo₂O₄ NPs as the HTL.

HTL	Scan direction	J_{SC} (mA/cm ²)	V_{OC} (V)	FF (%)	best PCE (%)	avg PCE^a (%)	R_S (Ω)
PEDOT:PSS film	Forward	16.27	0.6	54.67	5.3	5.18	257.97
	Reverse	16.27	0.8	63.73	8.29	7.86	128.15
ZnCo ₂ O ₄ NPs	Forward	20.06	0.88	66.82	11.78	11.27	109.39
	Reverse	19.85	0.92	67.19	12.31	11.55	94.51

^a Average PCE values were obtained from 20 devices.

4. Conclusions

In this study, we successfully synthesized ZnCo₂O₄ NPs by a facile chemical precipitation method, which were employed as the HTL in inverted PSCs. The obtained ZnCo₂O₄ NPs showed a spinel phase and an average particle size of 20 nm. The introduced NH₃ molecules were removed by annealing process to improve electrical properties of ZnCo₂O₄ NPs, as verified by FT-IR experiments. The Zn:Co atomic ratio of 1:2 and *p*-type transport character were confirmed by XPS observation. The downshifted VB level of ZnCo₂O₄ NPs is matched better with the perovskite absorbing layer to improve the hole extraction. Smoother ZnCo₂O₄ NPs layer was obtained by solution process with a low surface roughness of 6.65 nm, and larger sizes of perovskite grains were formed on the ZnCo₂O₄ NPs layer, as compared with PEDOT:PSS film. The optimized PSC based on the ZnCo₂O₄ NPs HTL exhibited a high PCE of 12.31%, negligible hysteresis, and excellent device stability of 240 hours storage under a halogen lamps matrix exposure in ambient environment. To date, the utilization of ZnCo₂O₄ NPs as the HTL provides a simple and effective approach to achieve PSCs with high efficiency and long-term stability that show promising use in photovoltaic application.

Abbreviations

HTL
hole transport layer
PSCs
perovskite solar cells
NPs

nanoparticles

PCE

power conversion efficiency

V_{OC}

open-circuit voltage

J_{SC}

short-circuit current density

FF

fill factor

PEDOT

PPS:poly(3,4-ethylenedioxythiophene):poly(styrene sulfonate)

PPN

poly(4,4'-bis(*N*-carbazolyl)-1,10-biphenyl)

PPP

poly (*p*-phenylene)

PT

polythiophene

FTO

fluorine-doped tin oxide

PC₆₁BM

[6,6]-phenyl-C₆₁-butyric acid methyl ester

TBABF₄

tetrabutylammonium tetrafluoroborate

PEI

polyethylenimine

ETL

electron transport layer

IPA

isopropyl alcohol

UV

ultraviolet

SEM

scanning electron microscope

AFM

atomic force microscope

TEM

transmission electron microscope

FT-IR

Fourier transform infrared

UPS
ultraviolet photoelectron spectroscopy
XPS
X-ray photoelectron spectroscopy
XRD
X-ray diffraction
PL
photoluminescence
TR-PL
time-resolved PL
J-V
current density-voltage
EQE
external quantum efficiency
 Φ_w
work function
 E_F
Fermi level
VB
valence band
 R_a
average roughness
 μ_h
hole mobility
 E_g
optical bandgap
CB
conduction band
LUMO
lowest-unoccupied molecular orbital
 R_s
series resistance
HI
hysteresis index.

Declarations

Availability of Data and Materials

The datasets generated and/or analyzed in this study are available from the corresponding author upon reasonable request.

Competing Interests

The authors declare that they have no competing interests.

Ethics Approval

Not applicable.

Funding

This work was supported by the Ministry of Science and Technology of the Republic of China under Contract No. MOST 110-2221-E-A49-082-MY3 and the Higher Education Sprout Project of the Ministry of Education (MOE) of the Republic of China.

Authors' Contributions

BR Jheng proposed the research idea, performed the experiments, and drafted the manuscript. PT Chiu participated in the device fabrication. SH Yang contributed to the data interpretation, manuscript writing, and supervised the research. YL Tong participated in the evaluation of devices. All authors read and approved the final manuscript.

Acknowledgements

Not applicable.

References

1. Kojima A, Teshima K, Shirai Y, Miyasaka T (2009) Organometal Halide Perovskites as Visible-Light Sensitizers for Photovoltaic Cells. *J Am Chem Soc* 131:6050–6051
2. National Renewable Energy Laboratory (NREL). Best research-cell efficiency chart. [Online]. <https://www.nrel.gov/pv/cell-efficiency.html> (2021-10-17).
3. Ball JM, Stranks SD, Hörantner MT, Hüttner S, Zhang W, Crossland EJW, Ramirez I, Riede M, Johnston MB, Friend RH, Snaith HJ (2015) Optical properties and limiting photocurrent of thin-film perovskite solar cells. *Energy Environ Sci* 8:602–609
4. Stranks SD, Eperon GE, Grancini G, Menelaou C, Alcocer MJP, Leijtens T, Herz LM, Petrozza A, Snaith HJ (2013) Electron-Hole Diffusion Lengths Exceeding 1 Micrometer in an Organometal Trihalide Perovskite Absorber. *Science* 342:341–344

5. Wang Y, Zhang Y, Zhang P, Zhang W (2015) High intrinsic carrier mobility and photon absorption in the perovskite $\text{CH}_3\text{NH}_3\text{PbI}_3$. *Phys Chem Chem Phys* 17:11516–11520
6. Miyata A, Mitoglu A, Plochocka P, Portugall O, Wang JTW, Stranks SD, Snaith HJ, Nicholas RJ (2015) Direct measurement of the exciton binding energy and effective masses for charge carriers in organic–inorganic tri-halide perovskites. *Nat Phys* 11:582–587
7. Eperon GE, Stranks SD, Menelaou C, Johnston MB, Herz LM, Snaith HJ (2014) Formamidinium lead trihalide: a broadly tunable perovskite for efficient planar heterojunction solar cells. *Energy Environ Sci* 7:982–988
8. Jacobsson TJ, Correa-Baena JP, Pazoki M, Saliba M, Schenk K, Grätzel M, Hagfeldt A (2016) Exploration of the compositional space for mixed lead halogen perovskites for high efficiency solar cells. *Energy Environ Sci* 9:1706–1724
9. Saliba M, Matsui T, Seo JY, Domanski K, Correa-Baena JP, Nazeeruddin MK, Zakeeruddin SM, Tress W, Abate A, Hagfeldt A, Grätzel M (2016) Cesium-containing triple cation perovskite solar cells: improved stability, reproducibility and high efficiency. *Energy Environ Sci* 9:1989–1997
10. Bu T, Liu X, Zhou Y, Yi J, Huang X, Luo L, Xiao J, Ku Z, Peng Y, Huang F, Cheng YB, Zhong J (2017) A novel quadruple-cation absorber for universal hysteresis elimination for high efficiency and stable perovskite solar cells. *Energy Environ Sci* 10:2509–2515
11. Meng L, You J, Guo TF, Yang Y (2016) Recent Advances in the Inverted Planar Structure of Perovskite Solar Cells. *Acc Chem Res* 49:155–165
12. Al-Ashouri A, Köhnen E, Li B, Magomedov A, Hempel H, Caprioglio P, Márquez JA, Vilches ABM, Kasparavicius E, Smith JA, Phung N, Menzel D, Grischek M, Kegelmann L, Skroblin D, Gollwitzer C, Malinauskas T, Jošt M, Matič G, Rech B, Schlatmann R, Topič M, Korte L, Abate A, Stannowski B, Neher D, Stolterfoht M, Unold T, Getautis V, Albrecht S (2020) Monolithic perovskite/silicon tandem solar cell with >29% efficiency by enhanced hole extraction. *Science* 370:1300–1309
13. Mantilla-Perez P, Feurer T, Correa-Baen JP, Liu Q, Colodrero S, Toudert J, Saliba M, Buecheler S, Hagfeldt A, Tiwari AN, Martorell J (2017) Monolithic CIGS–Perovskite Tandem Cell for Optimal Light Harvesting without Current Matching. *ACS Photonics* 4:861–867
14. You J, Yang Y, Hong Z, Song TB, Meng L, Liu Y, Jiang C, Zhou H, Chang WH, Li G, Yang Y (2014) Moisture assisted perovskite film growth for high performance solar cells. *Appl Phys Lett* 105:183902
15. Yan W, Li Y, Li Y, Ye S, Liu Z, Wang S, Bian Z, Huang C (2015) High-performance hybrid perovskite solar cells with open circuit voltage dependence on hole-transporting materials. *Nano Energy* 16:428–437

16. Yan W, Li Y, Li Y, Ye S, Liu Z, Wang S, Bian Z, Huang C (2015) Stable high-performance hybrid perovskite solar cells with ultrathin polythiophene as hole-transporting layer. *Nano Res* 8:2474–2480
17. Bießmann L, Kreuzer LP, Widmann T, Hohn N, Moulin JF, Müller-Buschbaum P (2018) Monitoring the swelling behavior of PEDOT:PSS electrodes under high humidity conditions. *ACS Appl Mater Interfaces* 10:9865–9872
18. Ahn S, Park MH, Jeong SH, Kim YH, Park J, Kim S, Kim H, Cho H, Wolf C, Pei M, Yang H, Lee TW (2019) Fine Control of Perovskite Crystallization and Reducing Luminescence Quenching Using Self-Doped Polyaniline Hole Injection Layer for Efficient Perovskite Light-Emitting Diodes. *Adv Funct Mater* 29:1807535
19. Sun H, Hou X, Wei Q, Liu H, Yang K, Wang W, An Q, Rong Y (2016) Low-temperature solution-processed p-type vanadium oxide for perovskite solar cells. *Chem Commun* 52:8099–8102
20. Zuo C, Ding L (2015) Solution-Processed Cu_2O and CuO as Hole Transport Materials for Efficient Perovskite Solar Cells. *Small* 11:5528–5532
21. You J, Meng L, Song TB, Guo TF, Yang YM, Chang WH, Hong Z, Chen H, Zhou H, Chen Q, Liu Y, De Marco N, Yang Y (2016) Improved air stability of perovskite solar cells via solution-processed metal oxide transport layers. *Nat Nanotechnol* 11:75–81
22. Bashir A, Shukla S, Lew JH, Shukla S, Bruno A, Gupta D, Baikie T, Patidar R, Akhter Z, Priyadarshi A, Mathews N, Mhaisalkar SG (2018) Spinel Co_3O_4 nanomaterials for efficient and stable large area carbon-based printed perovskite solar cells. *Nanoscale* 10:2341–2350
23. Thoka S, Chen CJ, Jena A, Wang FM, Wang XC, Chang H, Hu SF, Liu RS (2020) Spinel Zinc Cobalt Oxide (ZnCo_2O_4) Porous Nanorods as a Cathode Material for Highly Durable $\text{Li}-\text{CO}_2$ Batteries. *ACS Appl Mater Interfaces* 12:17353–17363
24. Huang Z, Ouyang D, Shih CJ, Yang B, Choy WCH (2019) Solution-Processed Ternary Oxides as Carrier Transport/Injection Layers in Optoelectronics. *Adv Energy Mater* 10:1900903
25. Ouyang D, Huang Z, Choy WCH (2019) Solution-Processed Metal Oxide Nanocrystals as Carrier Transport Layers in Organic and Perovskite Solar Cells. *Adv Funct Mater* 29:1804660
26. Ouyang D, Xiao J, Ye F, Huang Z, Zhang H, Zhu L, Cheng J, Choy WCH (2018) Strategic Synthesis of Ultrasmall NiCo_2O_4 NPs as Hole Transport Layer for Highly Efficient Perovskite Solar Cells. *Adv Energy Mater* 8:1702722
27. Lee JH, Jin IS, Noh YW, Park SH, Jung JW (2019) A Solution-Processed Spinel CuCo_2O_4 as an Effective Hole Transport Layer for Efficient Perovskite Solar Cells with Negligible Hysteresis. *ACS Sustainable Chem Eng* 7:17661–17670

28. Mercado CC, Zakutayev A, Zhu K, Flynn CJ, Cahoon JF, Nozik AJ (2014) Sensitized Zinc-Cobalt-Oxide Spinel p-Type Photoelectrode. *J Phys Chem C* 118: 25340–25349
29. Mandal B, Roy P, Mitra P (2020) Comparative study on organic effluent degradation capabilities and electrical transport properties of polygonal ZnCo_2O_4 spinels fabricated using different green fuels. *Mater Sci Eng C* 117:111304
30. Maity D, Karmakar K, Pal D, Saha S, Khan GG, Mandal K (2021) One-Dimensional p- ZnCo_2O_4 /n-ZnO Nanoheterojunction Photoanode Enabling Photoelectrochemical Water Splitting. *ACS Appl Energy Mater* 4:11599–11608
31. Huang L, Waller GH, Ding Y, Chen D, Ding D, Xi P, Wang ZL, Liu M (2015) Controllable interior structure of ZnCo_2O_4 microspheres for high-performance lithium-ion batteries. *Nano Energy* 11:64–70
32. Priya M, Premkumar VK, Vasantharani P, Sivakumar G (2019) Structural and electrochemical properties of ZnCo_2O_4 nanoparticles synthesized by hydrothermal method. *Vacuum* 167:307–312
33. Huang Z, Ouyang D, Ma R, Wu W, Roy VAL, Choy WCH (2019) A General Method: Designing a Hypocrystalline Hydroxide Intermediate to Achieve Ultrasmall and Well-Dispersed Ternary Metal Oxide for Efficient Photovoltaic Devices. *Adv Funct Mater* 29:1904684
34. Farhadi S, Pourzare K, Sadeghinejad S (2013) Simple preparation of ferromagnetic Co_3O_4 nanoparticles by thermal dissociation of the $[\text{Co}^{\text{II}}(\text{NH}_3)_6](\text{NO}_3)_2$ complex at low temperature. *J Nanostructure Chem* 3:16
35. *Silverstein, R. M.; Webster, F. X.; Kiemle, D. J. (2005) Spectrometric Identification of Organic Compounds, 7th Ed.; John Wiley and Sons: Hoboken, NJ, Ch.2.*
36. Luo W, Hu X, Sun Y, Huang Y (2012) Electrospun porous ZnCo_2O_4 nanotubes as a high-performance anode material for lithium-ion batteries. *J Mater Chem* 22:8916–8921
37. Kim TW, Woo MA, Regis M, Choi KS (2014) Electrochemical Synthesis of Spinel Type ZnCo_2O_4 Electrodes for Use as Oxygen Evolution Reaction Catalysts. *J Phys Chem Lett* 5:2370–2374
38. Mariappan CR, Kumar R, Prakash GV (2015) Functional properties of ZnCo_2O_4 nano-particles obtained by thermal decomposition of a solution of binary metal nitrate. *RSC Adv* 5:26843–26849
39. Chen HY, Chen PC (2020) P-type spinel ZnCo_2O_4 thin films prepared using sol-gel process. *Appl Surf Sci* 505:144460
40. Petitto SC, Langell MA (2004) Surface composition and structure of $\text{Co}_3\text{O}_4(110)$ and the effect of impurity segregation. *J Vac Sci Technol A* 22:1690–1696

41. Cole KM, Kirk DW, Thorpe SJ (2021) Co_3O_4 nanoparticles characterized by XPS and UPS. *Surf Sci Spectra* 28:014001
42. Navarro-Quezada A, Alamé S, Esser N (2015) Near valence-band electronic properties of semiconducting $\beta\text{-Ga}_2\text{O}_3$ (100) single crystals. *Phys Rev B* 92:195306
43. Tang H, Shang Y, Zhou W, Peng Z, Ning Z (2018) Energy Level Tuning of PEDOT:PSS for High Performance Tin-Lead Mixed Perovskite Solar Cells. *Sol RRL* 3:1800256
44. Ye X, Wen Z, Zhang R, Ling H, Xi J, Lu X (2021) High-performance and stable inverted perovskite solar cells using low-temperature solution-processed CuNbO_x hole transport layer. *J Power Sources* 483:229194
45. Zhang J, Luo H, Xie W, Lin X, Hou X, Zhou J, Huang S, Ou-Yang W, Sun Z, Chen X (2018) Efficient and ultraviolet durable planar perovskite solar cells via ferrocenecarboxylic acid modified nickel oxide hole transport layer. *Nanoscale* 10:5617–5625
46. Chang CC, Tao JH, Tsai CE, Cheng YJ, Hsu CS (2018) Cross-linked Triarylamine-Based Hole-Transporting Layer for Solution-Processed PEDOT:PSS-Free Inverted Perovskite Solar Cells. *ACS Appl Mater Interfaces* 10:21466–21471
47. Chiu PC, Yang SH (2020) Improvement in hole transporting ability and device performance of quantum dot light emitting diodes. *Nanoscale Adv* 2:401–407
48. Chandrasekhar PS, Seo YH, Noh YJ, Na SI (2019) Room temperature solution-processed Fe doped NiO_x as a novel hole transport layer for high efficient perovskite solar cells. *Appl Surf Sci* 481:588–596
49. Zhang H, Cheng J, Lin F, He H, Mao J, Wong KS, Jen AKY, Choy WCH (2016) Pinhole-Free and Surface-Nanostructured NiO_x Film by Room-Temperature Solution Process for High-Performance Flexible Perovskite Solar Cells with Good Stability and Reproducibility. *ACS Nano* 10:1503–1511
50. Zhang R, Liu D, Wang Y, Zhang T, Gu X, Zhang P, Wu J, Chen ZD, Zhao Y, Li S (2018) Theoretical lifetime extraction and experimental demonstration of stable cesium-containing tri-cation perovskite solar cells with high efficiency. *Electrochim Acta* 265:98–106
51. Dong S, Wan Y, Wang Y, Yang Y, Wang Y, Zhang X, Cao H, Qin W, Yang L, Yao C, Ge Z, Yin S (2016) Polyethylenimine as a dual functional additive for electron transporting layer in efficient solution processed planar heterojunction perovskite solar cells. *RSC Adv* 6:57793–57798
52. Zhou Y, Zhang X, Lu X, Gao X, Gao J, Shui L, Wu S, Liu JM (2019) Promoting the Hole Extraction with Co_3O_4 Nanomaterials for Efficient Carbon-Based CsPbI_2Br Perovskite Solar Cells. *Sol RRL* 3:1800315

Figures

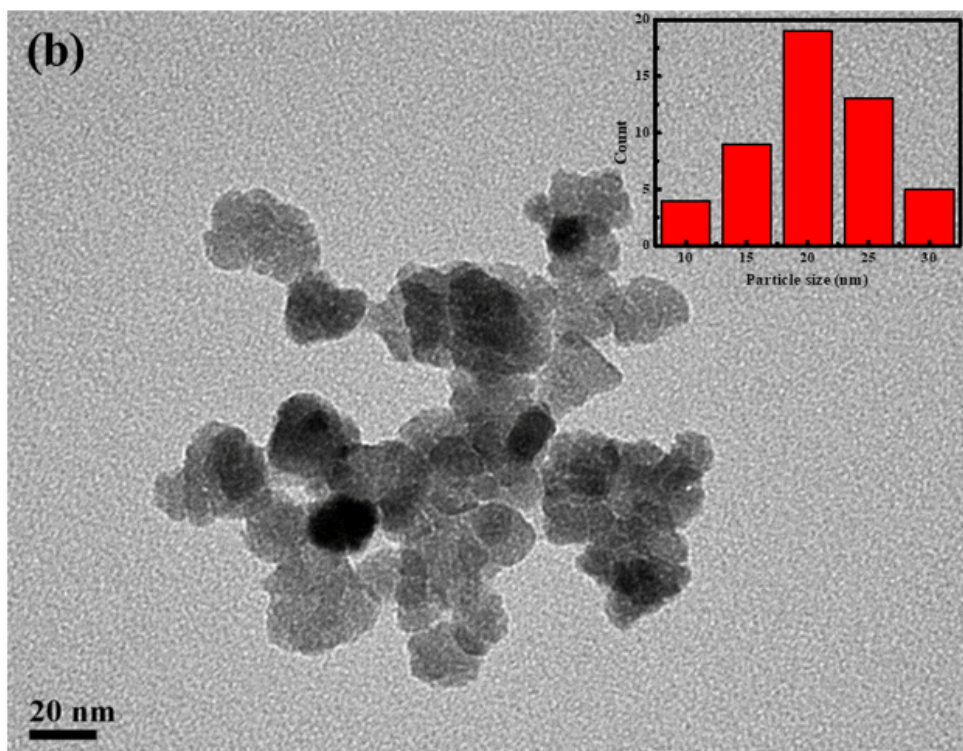
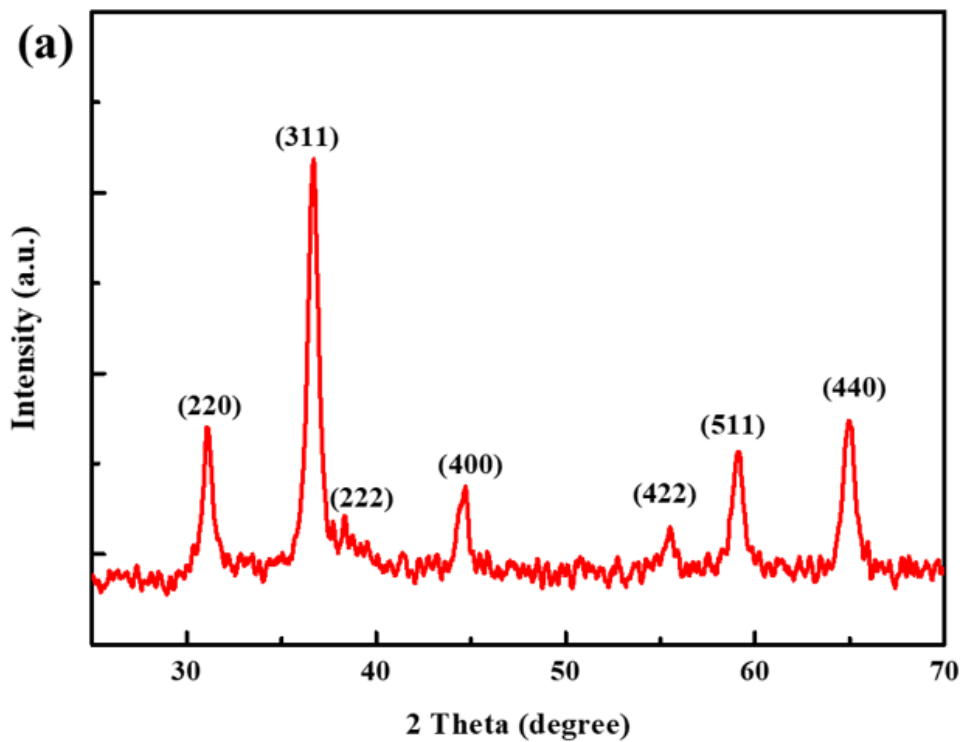


Figure 1

(a) XRD patterns and (b) TEM image of the ZnCo_2O_4 NPs. The inset shows the size distribution of NPs.

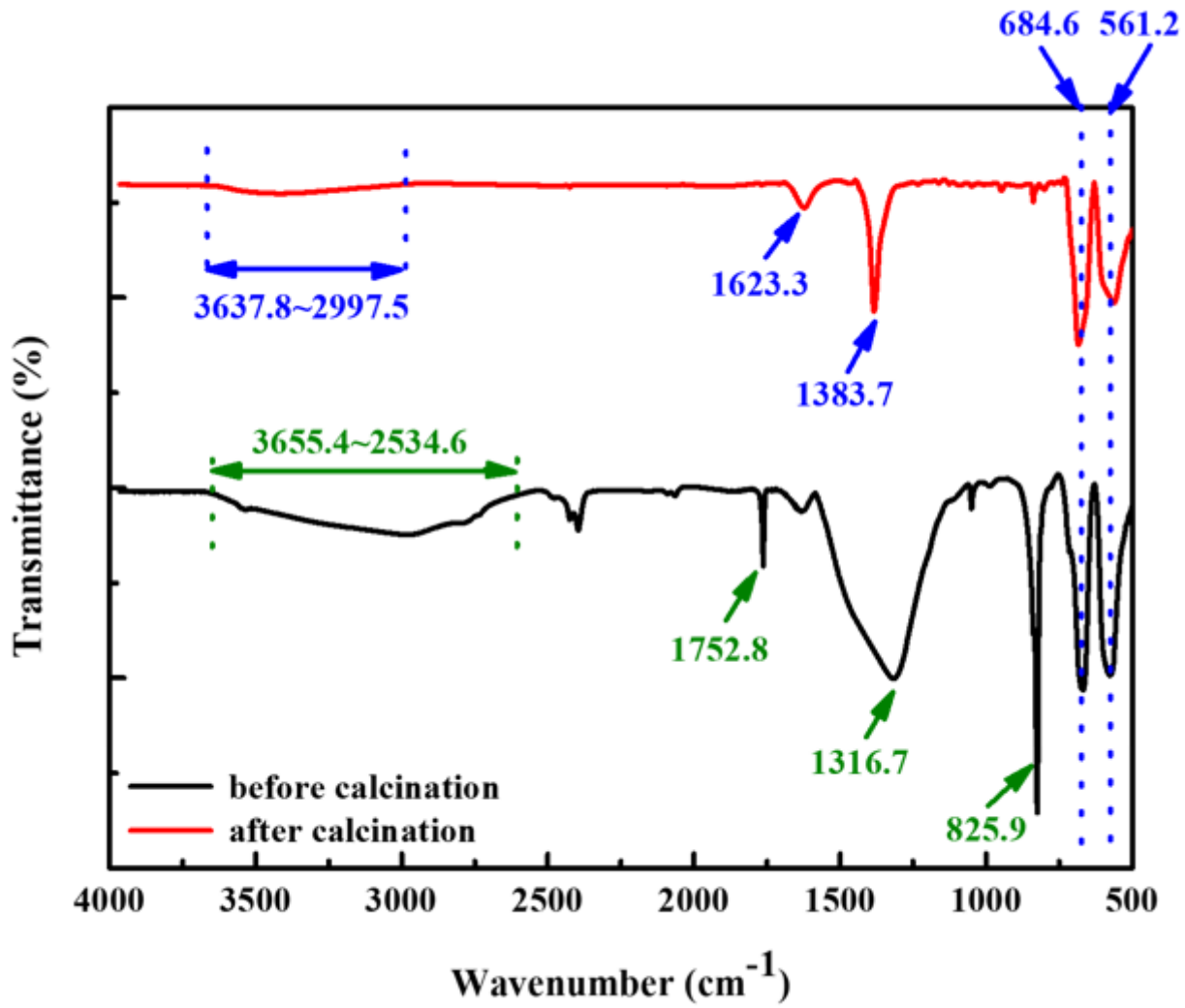


Figure 2

FT-IR spectra of the ZnCo₂O₄ NPs before and after calcination.

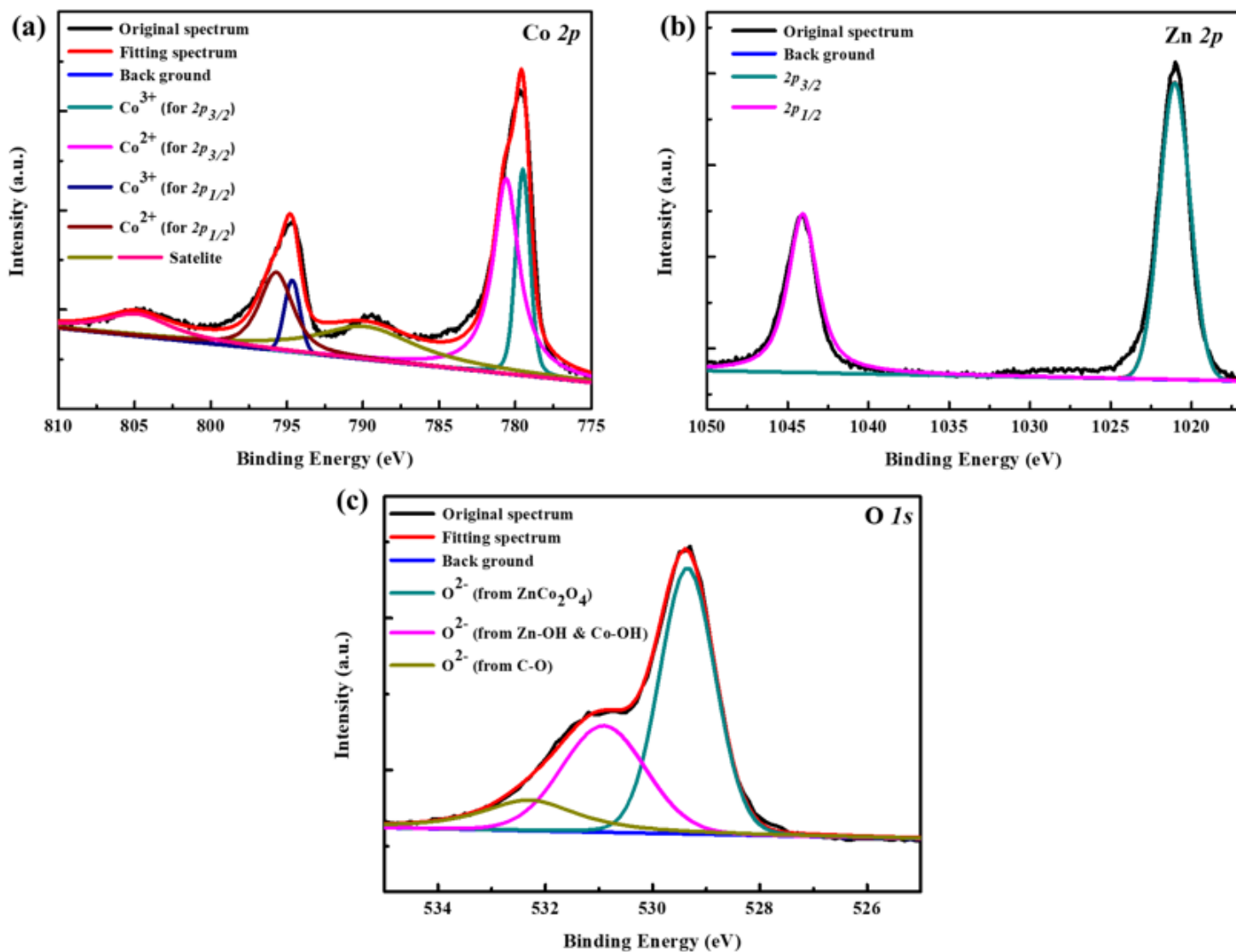


Figure 3

High-resolution XPS spectra of (a) Co 2p, (b) Zn 2p, and (c) O 1s elements in ZnCo₂O₄ NPs.

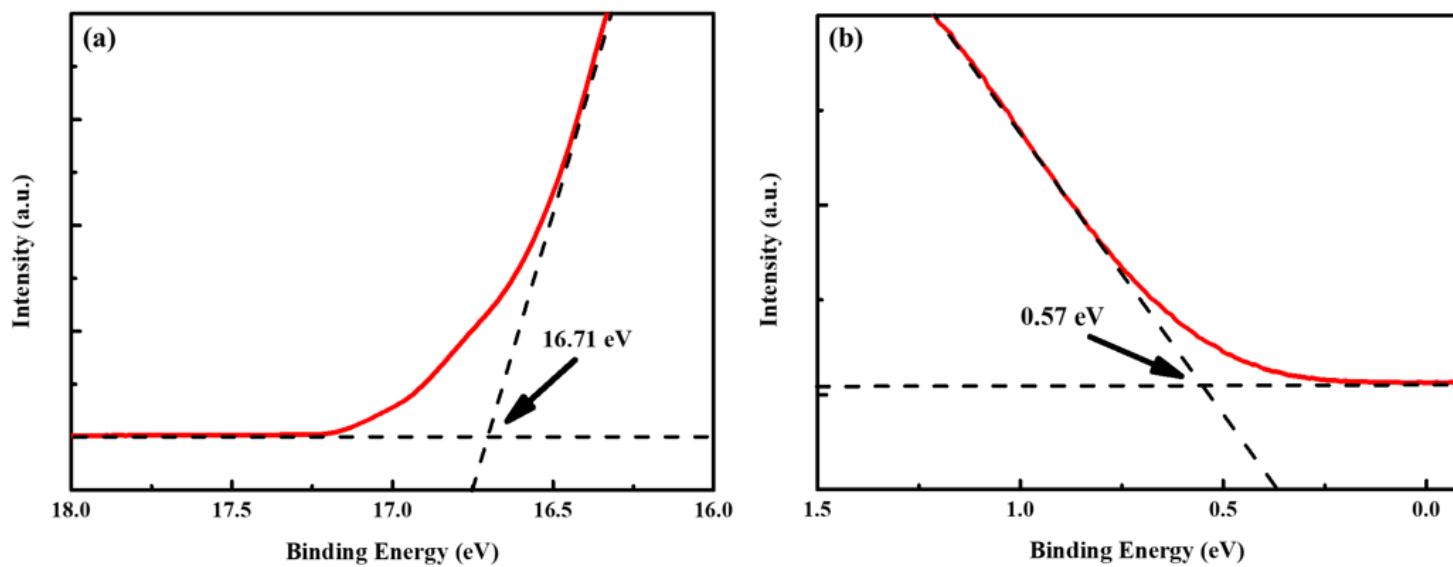


Figure 4

UPS spectra of ZnCo₂O₄ NPs at (a) high and (b) low binding energy regions.

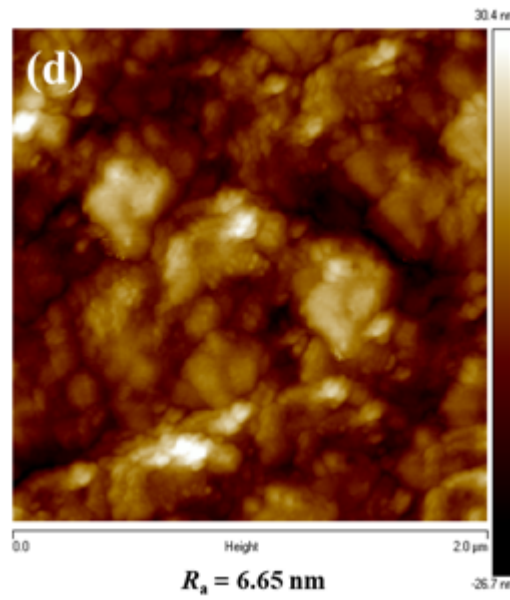
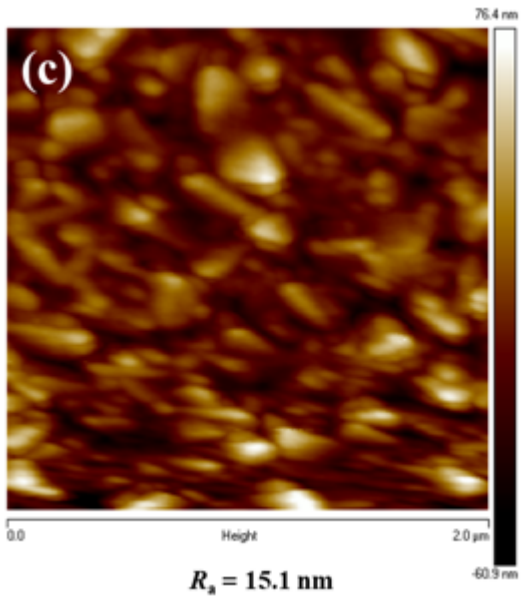
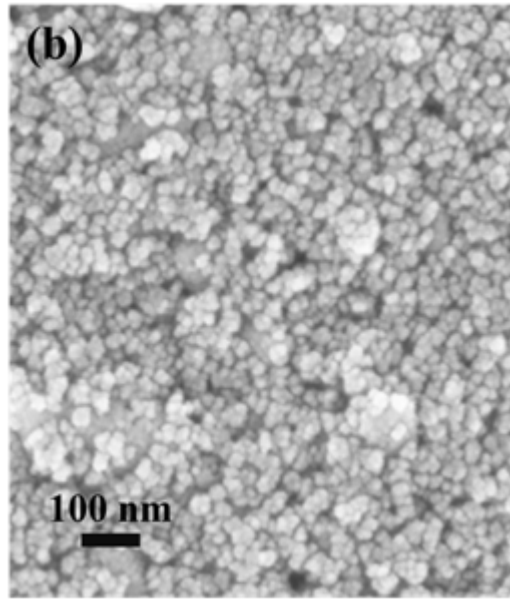
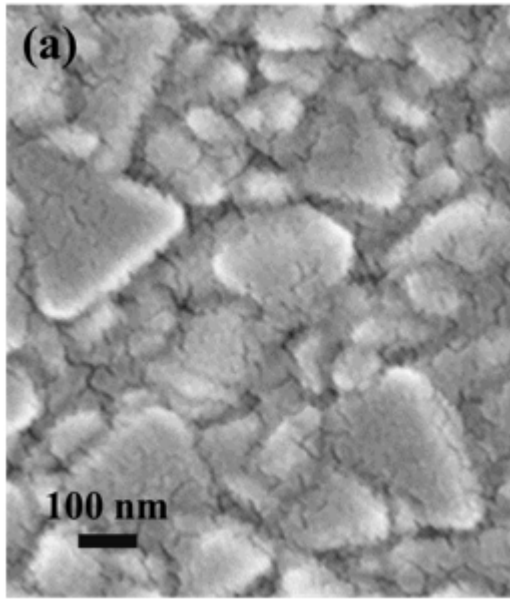


Figure 5

Top-view SEM and AFM topographic images of (a) (c) PEDOT:PSS film and (b) (d) ZnCo_2O_4 NPs layer deposited on FTO substrates.

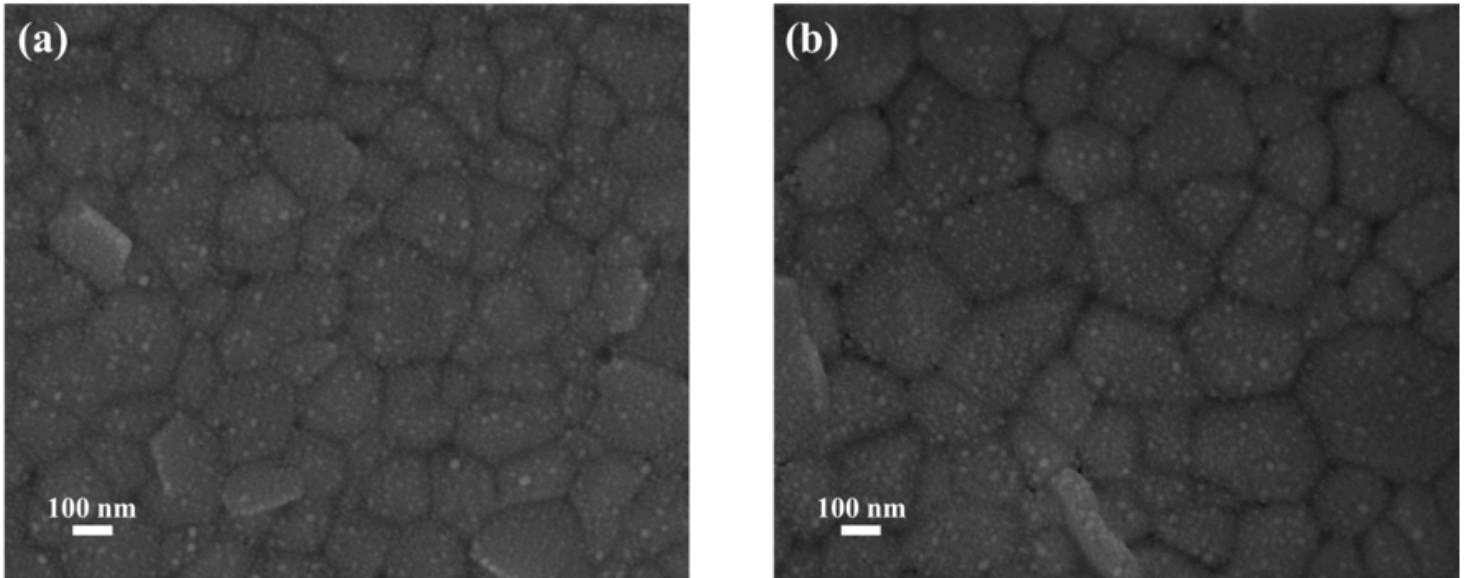


Figure 6

Top-view SEM images of the perovskite deposited on the (a) PEDOT:PSS thin film and (b) ZnCo_2O_4 NPs layer.

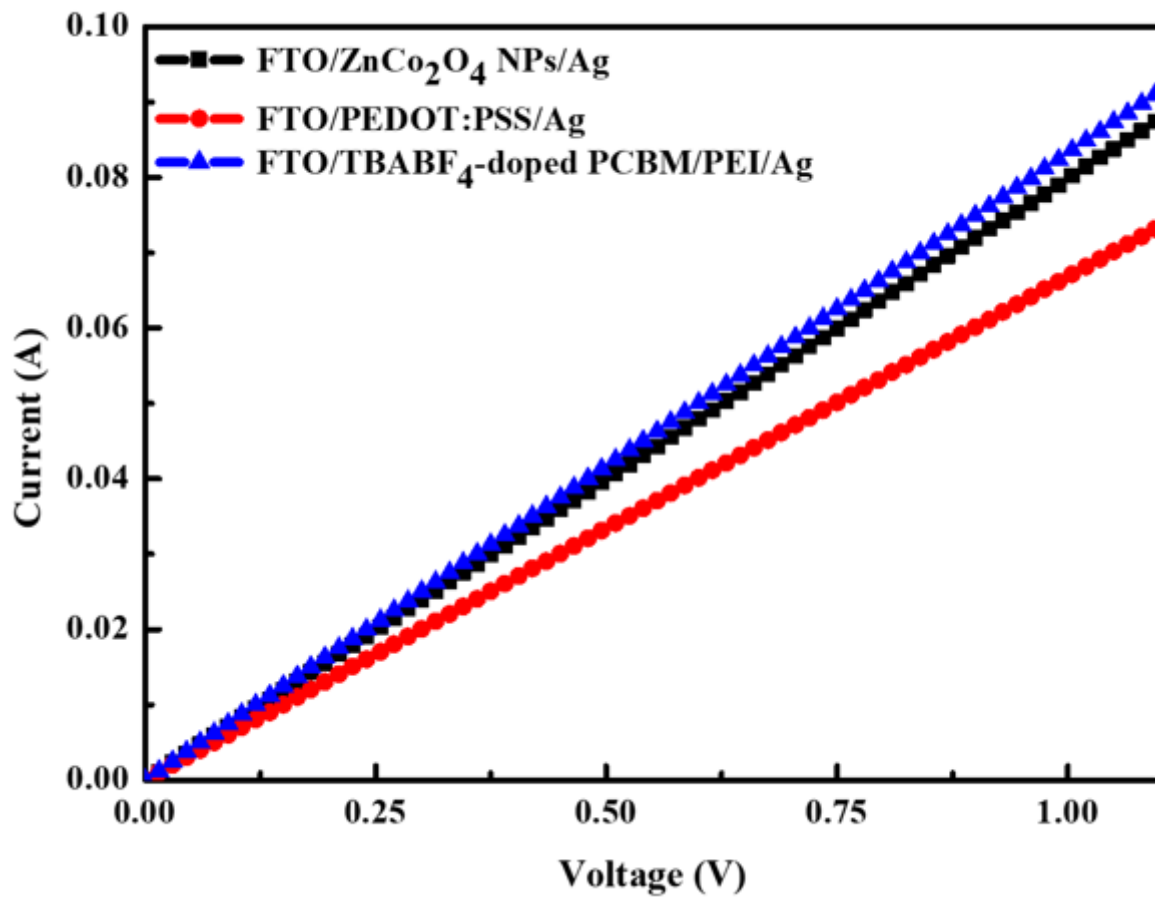


Figure 7

Current–voltage characteristics of hole-only devices FTO/ ZnCo_2O_4 NPs or PEDOT:PSS/Ag and electron-only device FTO/ TBABF_4 -doped PC_{67}BM /PEI/Ag.

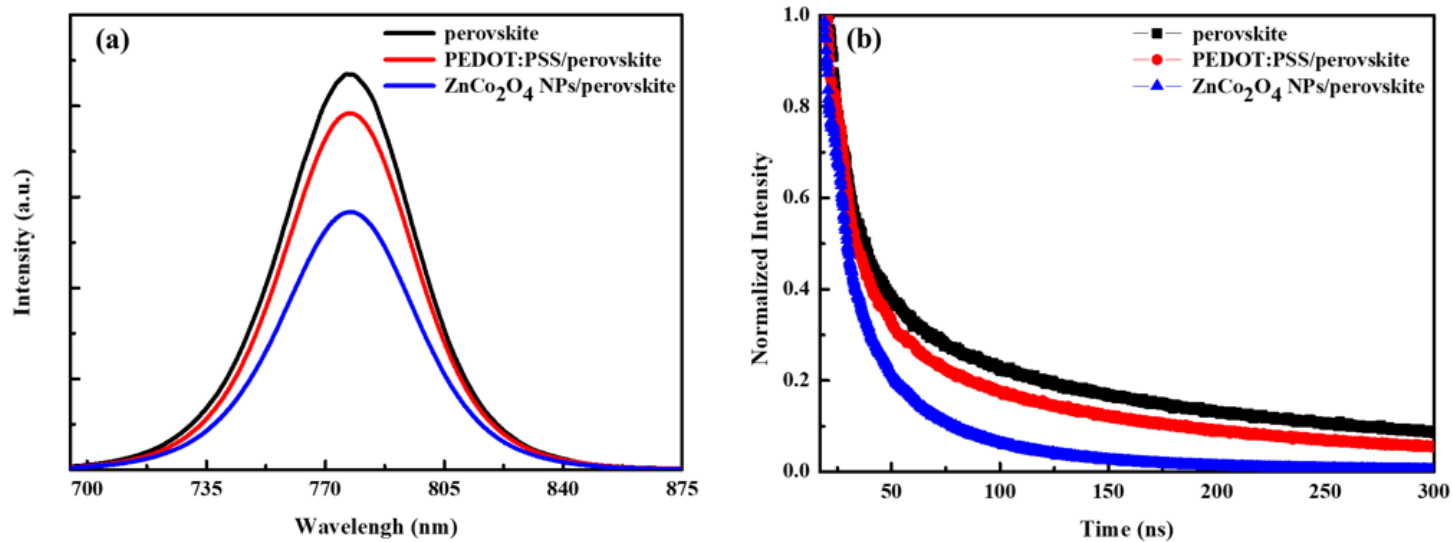


Figure 8

(a) PL emission spectra and (b) TR-PL decay curves of the perovskite on the FTO substrate, PEDOT:PSS film, and ZnCo_2O_4 NPs layer.

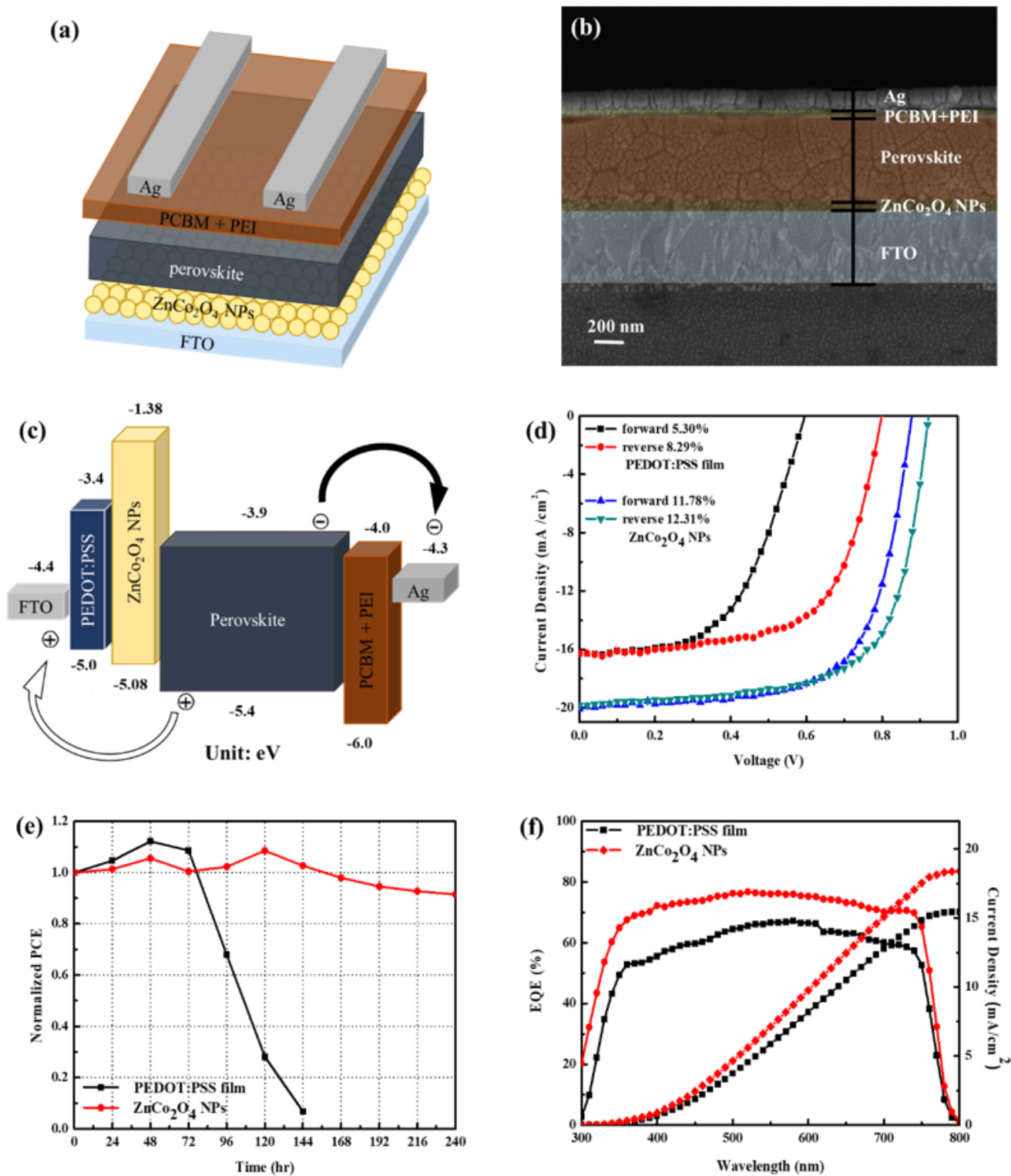


Figure 9

(a) Device structure and (b) cross-sectional SEM image of the PSC based on the ZnCo₂O₄ NPs layer; (c) energy level diagram of the whole device; (d) J-V characteristics, (e) normalized *PCE* evolution, and (f) EQE spectra and integrated current density of the PSCs based on PEDOT:PSS film or ZnCo₂O₄ NPs layer.

Supplementary Files

This is a list of supplementary files associated with this preprint. Click to download.

- [supplementaryInformationBRJheng.docx](#)